On the nature of planar defects in transition metal diboride line compounds

Justinas Palisaitis [a,*], Martin Dahlqvist [b], Lars Hultman [a], Ivan Petrov [a,c,d], Johanna Rosen [b], Per O.Å. Persson [a]

[a] *Thin Film Physics Division, Department of Physics, Chemistry and Biology (IFM), Linköping University, SE-581 83, Linköping, Sweden*
[b] *Materials Design Division, Department of Physics, Chemistry and Biology (IFM), Linköping University, SE-581 83, Linköping, Sweden*
[c] *Materials Research Laboratory, University of Illinois, Urbana, IL 61801, USA*
[d] *Department of Materials Science and Engineering, National Taiwan University of Science and Technology, Taipei 10607, Taiwan*

ARTICLE INFO

ABSTRACT

Planar defect structures appearing in transition metal diboride (TMB$_2$) thin films, grown by different magnetron sputtering-deposition approaches over a wide compositional and elemental range, were systematically investigated. Atomically resolved scanning transmission electron microscopy (STEM) imaging, electron energy loss spectroscopy (EELS) elemental mapping, and first principles calculations have been applied to elucidate the atomic structures of the observed defects. Two distinct types of antiphase boundary (APB) defects reside on the $\{1\bar{1}00\}$ planes. These defects are without (named APB-1) or with (APB-2) local deviation from stoichiometry. APB-2 defects, in turn, appear in different variants. It is found that APB-2 defects are governed by the film's composition, while APB-1 defects are endemic. The characteristic structures, interconnections, and circumstances leading to the formation of these APB-defects, together with their formation energies, are presented.

1. Introduction

Transition metal diborides (TMB$_2$) exhibit an appealing combination of functional properties that include high hardness, outstanding thermal stability, low wear rate, and high electrical conductivity [1–7]. This makes them suitable candidate materials in demanding applications for extreme environments [8–13]. Although boride containing phases possess high structural diversity, the hexagonal AlB$_2$ crystal structure (P6/mmm) is the most common for TMB$_2$. AlB$_2$ is characterized by a hexagonal structure in which close-packed layers of the TM atoms are interleaved by layers of boron (arranged in honeycombs) [14,15]. Many TMB$_2$ phases are known to be line compounds, that only form within a composition ratio of TM:B composition ratio of 1:2. Minor deviations from the perfect stoichiometry leads to formation of secondary phases and/or segregation of excess elements, which is the most common mechanism for B-rich TMB$_2$ films [5–18]. Attempts to grow TM-rich films remained a challenge for a long time, however, the recent success in the synthesis of such films has demonstrated that they, too, exhibit desirable properties like high hardness and oxidation resistance [19–26].

The presence of crystal imperfections in material structures plays an important role for its physical properties which can significantly affect the intended applications. The most common defects in thin films and coatings include point defects (impurities, vacancies) particularly in PVD sputtered films [27]. Additional defects include extended defects such as line- (e.g., dislocations), planar- (e.g., stacking faults, antiphase boundaries), and volumetric defects (inclusions) [28]. It has been reported that TMB$_2$ films possess stacking faults [19,29,30], metal-rich planar defects [31,32], and inclusions [7], while point defects have been addressed theoretically [33,34]. However, a systematic experimental and theoretical study to identify and systemize the types and atomic arrangements of extended planar defects, throughout the compositional and elemental range, is yet to be undertaken.

Driven by recent advances in synthesis of over- and understoichiometric TMB$_2$ films, it is essential to reveal and compare the atomic structure of formed structural defects, and by extension understand their influence of the material properties for future tailoring of application performance.

In this study, we employ advanced electron microscopy and theoretical methods to derive the atomic structure and chemistry of planar defects in TM-based diboride films. The description of defects in films throughout a wide elemental and compositional range are based on observations made in this manuscript and in previous investigations. Our collected findings have enabled us to identify the atomic configurations of observed antiphase boundary (APB) defects.

2. Experimental

The range of TMB$_2$ thin films were considered in terms of elemental composition (composition determination methods include Rutherford

---

* Corresponding author.
E-mail address: justinas.palisaitis@liu.se (J. Palisaitis).

Table 1
Summary of films considered in this study.

	Film	Composition	Synthesis	Refs.	Figs.
B/TM>2	$CrB_{2.10}$	RBS	DCMS	[20]	1a, 2a, S1a, S2,
	$ZrB_{2.40}$	ToF-ERDA	DCMS/HiPIMS	[29]	-
	$Ti_{0.79}Al_{0.21}B_{2.70}$	XPS	DCMS	[35]	S1b
	$TiB_{2.10}$	ToF-ERDA	DCMS	[30,36]	S1c
	$TiB_{2.40}$	ToF-ERDA	DCMS	[37]	-
B/TM<2	$Zr_{0.70}Ta_{0.30}B_{1.50}$	ToF-ERDA	DCMS and HiPIMS	[38]	-
	$CrB_{1.90}$	RBS	DCMS	[20]	1c, 2c, 4, 6, S3c
	$TiB_{1.44}$	ToF-ERDA/RBS	DCMS and HiPIMS	[19]	S3a
	$TiB_{1.90}$	RBS	DCMS	[31]	1b, 2b, S3b, S4, S5
	$TiB_{1.90}$	ToF-ERDA/RBS	DCMS and HiPIMS	[19]	S1d

Backscattering Spectrometry (RBS), time-of-flight elastic recoil detection analysis (ToF-ERDA), or X-ray photoelectron spectroscopy (XPS)) and synthesis method (direct-current magnetron sputtering (DCMS) and/or high-power-impulse-magnetron-sputtering (HiPIMS)) with corresponding references are summarized in Table 1. Films presented in the manuscript include $CrB_{1.90}$, $CrB_{2.10}$, and $TiB_{1.90}$ [20,31].

For STEM analysis, plan-view samples were prepared by a combined approach that includes mechanical and ion sample treatments to achieve electron transparency, as described elsewhere [39].

The thin film sample microstructure and elemental distribution were explored at the atomic scale using high angle annular dark field STEM (HAADF-STEM), annular bright field (ABF-STEM) imaging, selective area electron diffraction (SAED), and electron energy-loss spectroscopy (EELS). Characterization was performed using the Linköping double Cs corrected FEI Titan³ 60-300, operated at 300 kV. Atomically-resolved HAADF-STEM imaging was performed by using a 21.5 mrad convergence semi-angle, which provided sub-Ångström resolution probes with ~ 80 pA beam current. The HAADF-STEM images were recorded using an angular detection range of 46–200 mrad. HAADF-STEM is a dark field (DF) imaging method where atomic columns appear bright (on a dark background). The signal intensity of the atomic columns in HAADF-STEM images are referred to as directly interpretable and proportional to atomic number ($\sim Z^{1.7}$) and sample thickness. While HAADF-STEM imaging is widely applied, light element detection is limited due to the weak electron-scattering power of light elements [40].

In contrast, ABF-STEM imaging is a bright-field (BF) imaging method where atomic columns appear dark (on a bright background) and enable visualization of atomic columns from both relatively heavy (TMs, etc.) and light (B, etc.) elements simultaneously, due to contribution of lower-angle scattered electrons as compared to HAADF [41]. The ABF-STEM images were recorded using an angular detection range of 9–21 mrad.

STEM-EELS spectrum images of 30×50 pixels were acquired for 1 min using a 0.25 eV/channel energy dispersion, 0.2 s pixel dwell time, and a 55 mrad collection semi-angle of the employed Gatan Quantum ERS post-column imaging filter. Elemental B, Ti and Cr distribution maps were extracted from the spectrum images by background subtraction, using a power law, and choosing characteristic edge energy loss integration windows for B-K (188-208 eV), Ti-L_{23} (455-470 eV), and Cr-L_{23} (575-590 eV).

All first-principles calculations were performed by means of density functional theory (DFT) and the projector augmented wave method [42,43], as implemented within the Vienna *ab-initio* simulation package (VASP) version 5.4.1 [44–46]. The generalized gradient approximation (GGA), as parameterized by Perdew–Burke–Ernzerhof (PBE) [47], was used for treating the electron exchange and correlation effects. A plane-wave energy cut-off of 400 eV was used and the Brillouin zone was integrated by Monkhorst–Pack special k-point sampling with a density of 0.1 Å^{-1} [48]. The total energy is minimized through relaxation of unit-cell shape, volume, and internal atomic positions until satisfying an energy convergence of 10^{-7} eV/atom and force convergence of 10^{-2} eV/Å.

The thermodynamic stability has been investigated at 0 K with respect to decomposition into any combination of competing phases. The set of most competing phases at given composition, also known as equilibrium simplex, is identified using a linear optimization procedure [49,50]. The stability of a phase is quantified in terms of the formation enthalpy ΔH_{cp} by comparing its energy to the energy of the equilibrium simplex according to Eq. (1)

$$\Delta H_{cp} = E(TMB_{2-x}) - E(equilibrium\ simplex). \tag{1}$$

A phase is concluded stable when $\Delta H_{cp} < 0$.

In addition, the B vacancy formation energy expressed as energy change per defect created was calculated using to Eq. (2)

$$\Delta E_{vac} = \left[E(TMB_{2-x}) - E(TMB_2) + xE(B) \right]/x, \tag{2}$$

where $E(TMB_{2-x})$, $E(TMB_2)$ and $E(B)$ is the total energy per formula unit for TMB_{2-x}, TMB_2 and B, respectively.

3. Results and discussion

3.1. Experimental results

Independent of the deposition method, synthesized TMB_2 thin films typically exhibits a pronounced columnar growth along the [0001] direction. This makes plan-view STEM investigations (along [0001]) the preferred choice due to ability to examine individual features (e.g., boundaries and defects) along their extension throughout the grown film without projection of overlapping grains. Plan-view STEM imaging of the samples along [0001] was performed on the films summarized in Table 1. Overview images together with corresponding SAED patterns (shown in the insets) from the highest crystal quality near-stoichiometric TMB_2 films: $CrB_{2.1}$, $TiB_{1.9}$, and $CrB_{1.9}$ are displayed in Fig. 1a, 1b, and 1c, respectively. Those films are the main foci of this investigation as they enabled detailed examination of individual extended defects at the atomic scale. Matching plan-view STEM observations from the other films, comprising a wide compositional and elemental range, are shown in Figs. S1–S5 and in Refs. [29,37, 38].

Fig. 1a shows the HAADF-STEM image of the overstoichiometric $CrB_{2.1}$ film containing dark contrast regions - up to 20 nanometers in diameter - corresponding to an average low-atomic number that indicate B-rich and Cr-deficient inclusions as confirmed by EELS and reported elsewhere [20]. The excess boron segregation to these nanocolumnar grain boundaries or formation of a B-rich amorphous tissue phase is a well-known phenomenon [5]. B-segregation was observed in all investigated overstoichiometric TMB_2 films, see Fig S1. Otherwise, no other apparent defects are visible at lower magnification in the $CrB_{2.1}$ film.

Fig. 1b and c show HAADF-STEM images of the understoichiometric $TiB_{1.9}$ and $CrB_{1.9}$ films, respectively. In both cases B-rich inclusion are absent in the films. The films, however, exhibit a range of planar defects of different appearances which are visible as the bright contrast lines. The planar defects are residing on the {1$\bar{1}$00} prismatic planes, in line with previous reports [20,31].
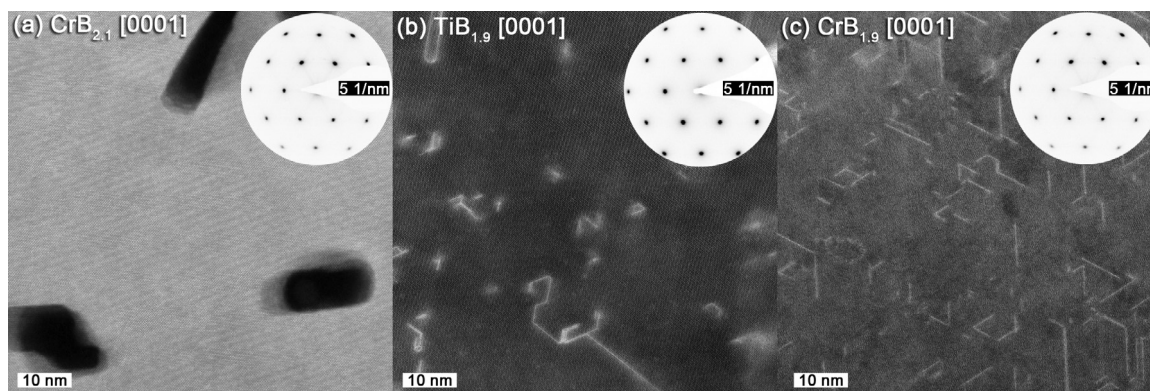
Fig. 1. HAADF-STEM images showing the microstructure of (a) $CrB_{2.1}$, (b) $TiB_{1.9}$, and (c) $CrB_{1.9}$, thin film along a plan-view [0001] zone axis. The insets show corresponding SAED patterns.
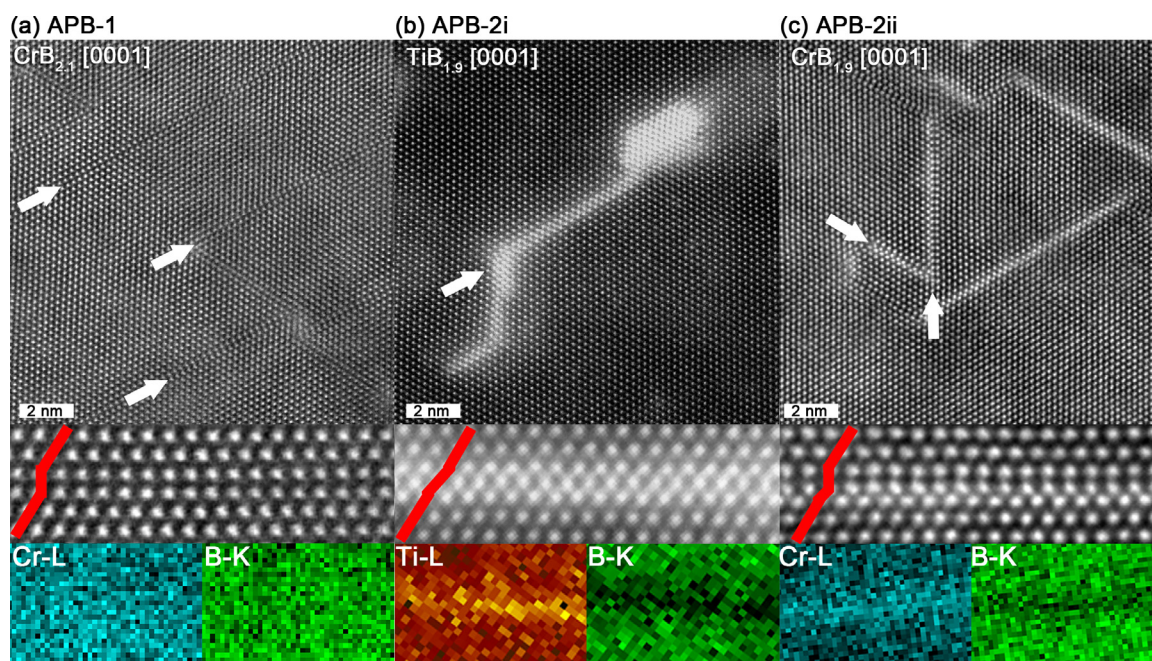

Fig. 2. Atomically-resolved plan-view HAADF-HRSTEM images acquired from planar defects in (a) $CrB_{2.1}$, (b) $TiB_{1.9}$, and (c) $CrB_{1.9}$, thin films. The planar defect arrangement is highlighted in the magnified lower images together with B, Ti, and Cr EELS elemental maps.

The plan-view SAED patterns, shown as insets in Fig. 1, accentuates the high-crystal quality by the discrete hexagonal pattern, corresponding to the AlB_2 crystal structure along the [0001] zone axis.

Fig. 2 shows the atomically-resolved plan-view HAADF-STEM images and EELS elemental maps of characteristic planar defects in $CrB_{2.1}$ (Fig. 2a), $TiB_{1.9}$ (Fig. 2b), and $CrB_{1.9}$ (Fig. 2c), and highlighted by arrows in the figures. Note that the contrast from the defects is distinctly different between the planar defects in the overstoichiometric sample compared to the understoichiometric samples.

The investigated films (Figs. 1, 2, S1–S5) contained various types of uniformly distributed planar defects, exhibiting atomically sharp confinements to the surrounding lattices confirming their planar nature along the growth direction, with variation in appearance, configuration, and structure. All planar defects reside on the $\{1\bar{1}00\}$ prismatic planes of the AlB_2 crystal structure.

The defects observed in this work can be classified according to previous investigations [51–54] as antiphase boundaries (APB): Type 1 (conservative APB-1) and Type 2 (non-conservative APB-2). APB-1 is defined by a lattice translation in the boundary plane and there is no net increase or decrease in the number of atoms at the interface (no

compositional change) as observed experimentally (Fig. 2a) and considered theoretically (Fig. 3a). In contrast, APB-2 is defined by a lattice translation in the boundary plane together with a net change in the number of atoms at the interface (compositional change). In addition, APB-2 type boundaries can assume three different atomic arrangements out of which two were observed experimentally (Fig. 2b-c). All three APB-2 were considered theoretically (Fig. 3b-d), which require introduction and definition of APB-2 subtypes, referred as APB-2i, APB-2ii, and APB-2iii.

According to their characteristic features, the experimentally observed defects were identified as APB-1 (Fig. 2a), APB-2i (Fig. 2b), and APB-2ii (Fig. 2c), as defined below:

APB-1:

Fig. 2a shows the presence of APB-1 defects distributed in $CrB_{2.1}$ along the $\{1\bar{1}00\}$ facets. The stacking sequence across APB-1 defects is featuring a half-unit cell $(1/2)a[11\bar{2}0]$ parallel shift of the structure and with respect to adjacent regions, thus acting as a mirror plane when viewed along [0001] in the otherwise ordered CrB_2 structure. APB-1 is a conservative APB, i.e., a lattice translation in the boundary plane with no net increase or decrease in the number of atoms at the inter-
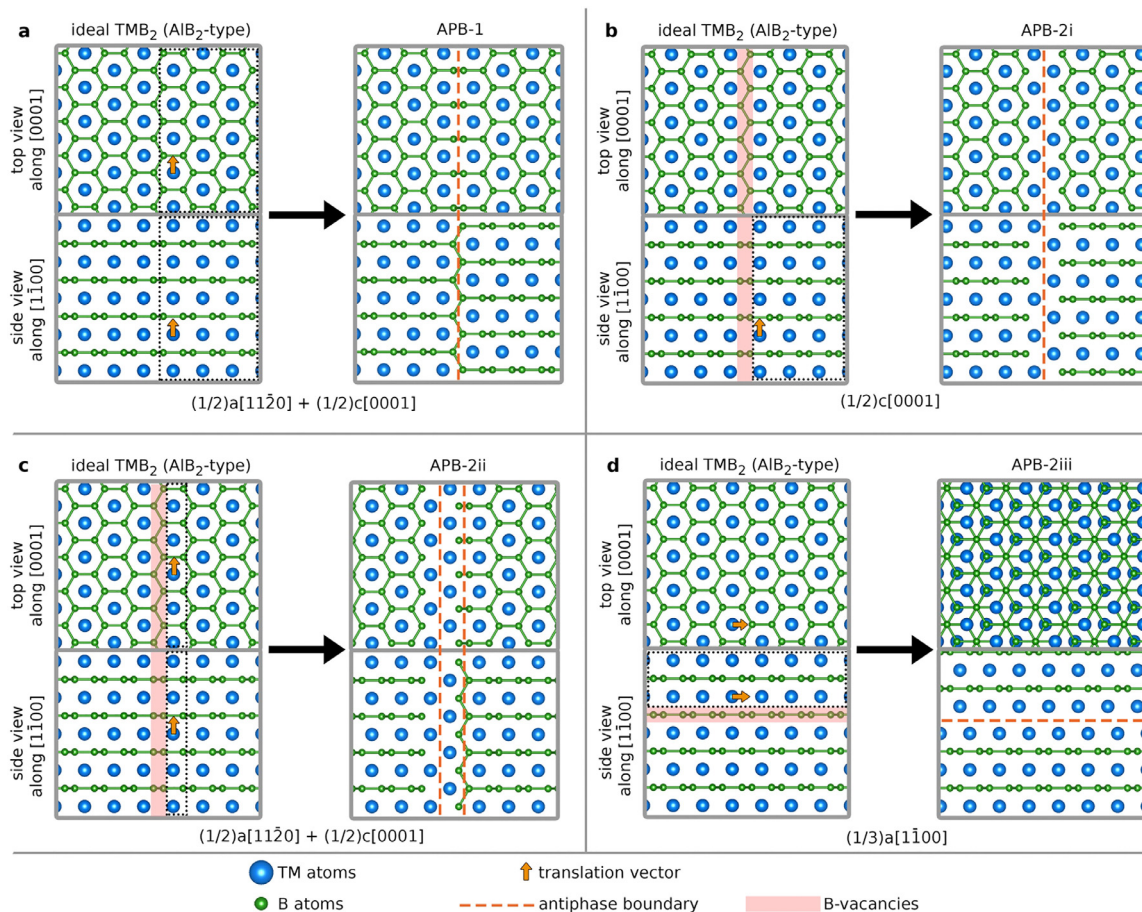
Fig. 3. Schematic illustration of different APBs considered for TMB_2 with AlB_2-type structure, with the translation vector (orange arrow) showing when passing the interface boundary. (a) APB-1 being conservative with no net change in composition at the interface and (b-d) APB-2 being non-conservative with a net change in the number of atoms at the interface. Red shaded area mark atoms in the ideal TMB_2 which are vacant in the corresponding APB-2 structures.

face. This is corroborated by no compositional fluctuation observed in the defect as evidenced from the EELS data. This type of defect is the most common planar defect, as observed throughout all here investigated TMB_2 thin films, see Figs. S1–S3. This implies that the presence of APB-1 defects is independent of transition metal, film composition, and growth method. Indeed, this type of defect, generally assigned as stacking faults (SFs) or grown-in planar faults, were previously observed in some TM films [19,29,30,32] although without detail structural identification. Fast Fourier Transform (FFT) analysis shows the presence of edge dislocations associated with accommodation of APB-1 defects in high crystal quality $CrB_{2.1}$ film (Fig. S2). It should be noted that the presence of APB-1 defects is not visible at low magnification STEM imaging (Fig. 1a), as such defects has no compositional change from surrounding, and lattice resolved imaging is required to resolve their stacking (Fig. 2a).

APB-2i:

Fig. 2b shows the presence of APB-2i defects distributed in $TiB_{1.9}$ along the $\{1\bar{1}00\}$ facets in agreement with previous report [31]. APB-2i defects are Ti-rich and B-deficient as evidenced from EELS maps. The B-deficiency in the defect region is consistent with a non-conservative APB as defined by a lattice translation in the boundary plane and a net change in the number of atoms at the interface. The formation of TM-rich APB-2i defects is associated to the accommodation of the lack of B-atomic planes in understoichiometric films causing lattice contraction at the defect sites if compared to the surrounding lattice as visualized in Fig. S6. As mentioned above, HAADF-STEM image contrast is commonly referred to as directly interpretable Z contrast [40]. However, such in-

terpretation of HAADF-HRSTEM image contrast can be problematic as one need to account for the complex electron-channelling phenomena inside the structures [55]. The bright contrast from the APB-2i defects is caused mainly by the compressively strained lattice at APB-2i defect sites (see Fig. S6) resulting in additional intensity (to medium scattering angles) under the applied imaging conditions. To illustrate the APB-2i defect visibility dependence on the imaging conditions, a HAADF-HRSTEM camera length series was recorded and is shown in Fig. S7. As can be seen, the bright contrast associated with the APB-2i defect can be greatly reduced for short camera lengths (allowing only high scattering angles) where the strain contribution is significantly decreased. TM-rich APB-2i defects were observed exclusively in understoichiometric TM diboride films as illustrated in Fig. S3. It should be noted that the presence of APB-2i defects is visible already during low magnification STEM imaging (Fig. 1b).

APB-2ii:

Fig. 2c shows the side-by-side coexistence of APB-1 and APB-2i defects (denoted as APB-2ii) distributed in $CrB_{1.9}$. In agreement with the description above, the APB-2ii defects are Cr-rich and B-deficient on the APB-2i defect side as evidenced from the corresponding EELS map. APB-2ii defects was only observed in understoichiometric TMB_2, in agreement with prerequisites of B-deficiency for the formation of APB-2 type defects, as illustrated also for $TiB_{1.9}$ in Fig. S4. It should be noted that the indications of combined APB-2ii defects are visible already during low magnification STEM imaging (Fig. 1c), however, atomic-resolution STEM imaging is required to distinguish between APB-2i and combined APB-2ii (Fig. 2b-c).
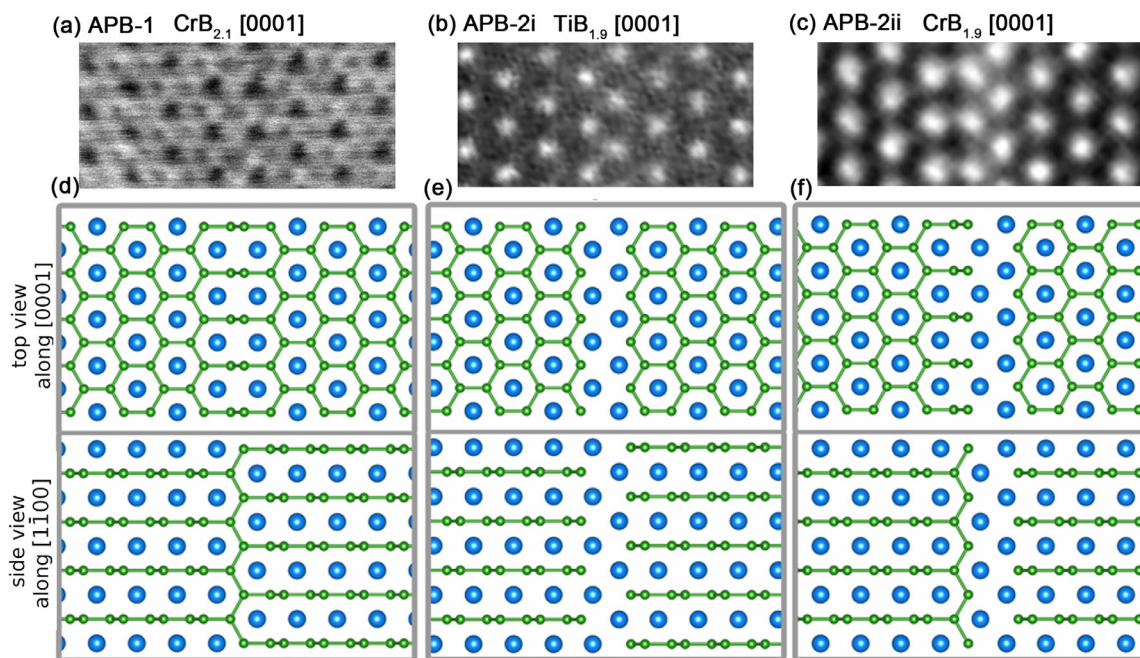
Fig. 4. Atomically-resolved plan-view images acquired from APB defects in (a) $CrB_{2.1}$ (ABF-HRSTEM), (b) $TiB_{1.9}$ (HAADF-HRSTEM), and (c) $CrB_{1.9}$ (HAADF-HRSTEM), thin films. Relaxed atomic structure models in top-view [0001] and side-view [$1\bar{1}00$] of corresponding APB defects in (d) $CrB_{2.1}$, (e) $TiB_{1.9}$, and (f) $CrB_{1.9}$. (d-f) Corresponding relaxed atomic structure models in top-view [0001] and side-view [$1\bar{1}00$] of APB defects.

3.2. Theoretical results

To theoretically investigate the planar defects observed in Fig. 2, atomic models of the APB defects were generated based on the experimental observations. Various combinations of planar defects are considered under relaxed conditions.

Fig. 3 shows a schematic illustration of the different APBs considered for TMB_2 and their relation to the ideal structure. APB-1 is characterized by a crystal translation $(1/2)a[11\bar{2}0]+(1/2)c[0001]$, shown in Fig. 3a. Three different APBs of type 2 (APB-2) have been considered, and they are characterized by a crystal translation along $(1/2)c[0001]$ combined with removal of a ($1\bar{1}00$) B-plane (Fig. 3b, denoted APB-2i), a crystal translation along $(1/2)a[11\bar{2}0]+(1/2)c[0001]$ combined with removal of a ($1\bar{1}00$) B-plane (Fig. 3c, denoted APB-2ii) and a crystal translation along $(1/3)a[1\bar{1}00]$ combined with removal of a (0001) B-plane (Fig. 3d, denoted APB-2iii).

Fig. 4 shows direct comparison of the experimentally obtained ABF-STEM (Fig. 4a) and HAADF-HRSTEM (Fig. 4b-c) images side-by-side with APB-1 (Fig. 4a), APB-2i (Fig. 4b) and APB-2ii (Fig. 4c) defects' model atomic structures. Note that the ABF-STEM image (Fig. 4a) possess BF contrast compared with the DF contrast in HAADF-HRSTEM images (Fig. 4b-c) as further detailed in experimental section. There is a good agreement between the HRSTEM images and the proposed atomic structure models of the APB defects.

Even though we did not find experimental evidence for the APB-2iii defect structure (Fig. 3d), it is included in our APB theoretical comparison (Fig. 3), since it is the most favorable APB for some systems, like ZrB_2 and HfB_2 (see Fig. 5).

Fig. 5 shows the calculated formation enthalpy, ΔH_{cp}, as function of the antiphase boundary distance, here expressed as inverse (1/d), where a value of zero represent infinite distance between the boundaries, i.e., ideal TMB_2. A phase is considered thermodynamically stable when $\Delta H_{cp} \leq 0$.

Hence, the stability presented in Fig. 5 demonstrate that the formation of an APB in many systems is energetically neutral as seen from ΔH_{cp} being unchanged for various APB distances (see APB-2i for TiB_2, VB_2, NbB_2). In some systems, the formation of APB is favorable as in-dicated by a decrease in ΔH_{cp}, shown for APB-2i in TaB_2. APB defects was intentionally not investigated for CrB_2 since this phase is magnetic [56] and its magnetic nature requires modeling a range of magnetic configurations at APB, which is beyond the scope of this work.

It should be noted that APB-1, APB2-i and APB-2ii is closely related. From the results in Fig. 5, it can be understood that the presence of APB-2i and APB-2ii is one way for the system to accommodate understoichiometry. This stands in contrast to APB-1, which act as way to restore the film planes to be coherent with other planes of the film. The combination, or simultaneous presence, of different APBs is demonstrated in Fig. 6 where three defects interconnect (see also Fig. S5).

For APB defects to form interconnection(s) one needs to consider the lattice shift along [0001] direction (along c-axis) across the APB defects. This change is illustrated in Fig. 3 while observing the structures in the side-view (along [$1\bar{1}00$]). For APB-1 and APB-2i the lattice shifts by 1/2c across the defect, while for APB-2ii the lattice undergoes no shift. This leads to several possible APB interconnections with 3- and 2-way configurations as illustrated in Fig. 7.

An interconnection between various APBs configurations can be making 120° (Fig. 6) or 60° (Fig. 2a,c) angles.

4. Conclusions

Planar defects in TMB_2 thin films for a range of TMs at a varying stoichiometry (B/TM), from 1.4 to 2.7 were investigated through a combination of the advanced microscopy and theoretical modeling. Two kinds of antiphase boundaries were identified; APB-1 is characterised by a lattice translation in the boundary plane without compositional change, while APB-2 shows a lattice translation together with a compositional change. In addition, three subtypes of APB-2 defects were considered theoretically, of different atomic configurations, and two of these were observed in experiments. It is concluded that APB-1 type defects appear independently in all films, while APB-2 defects are only present in understoichiometric films where their formation is promoted by an excess of TM. The simulations revealed no constraints for APB defect formation in TMB_2 thin films and indicated their closely related atomic configura-
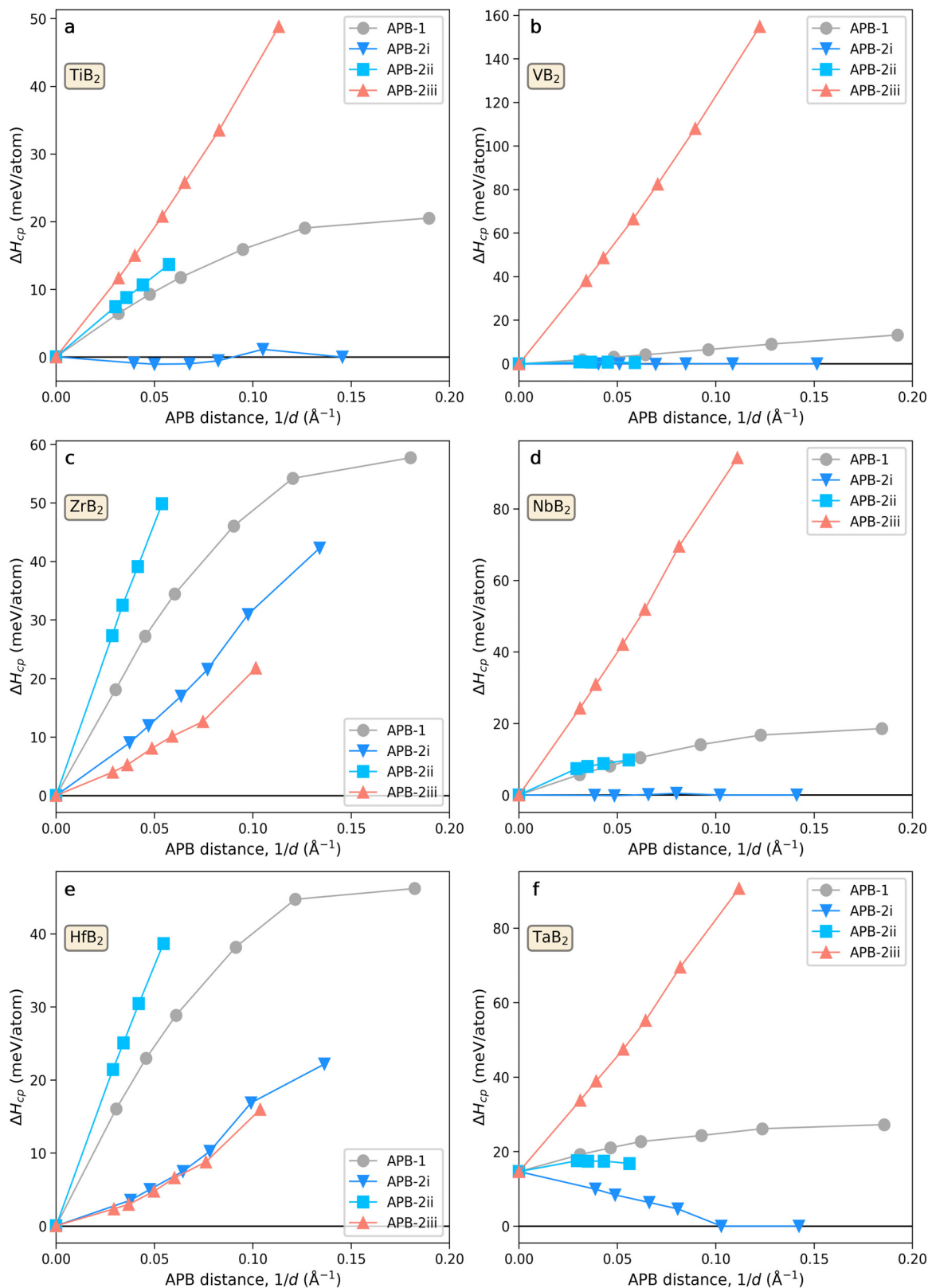
Fig. 5. Calculated formation enthalpy as function of the inverse antiphase boundary distance for six different TMB_2 phases considering conservative (APB-1) and non-conservative (APB-2) planar defects.
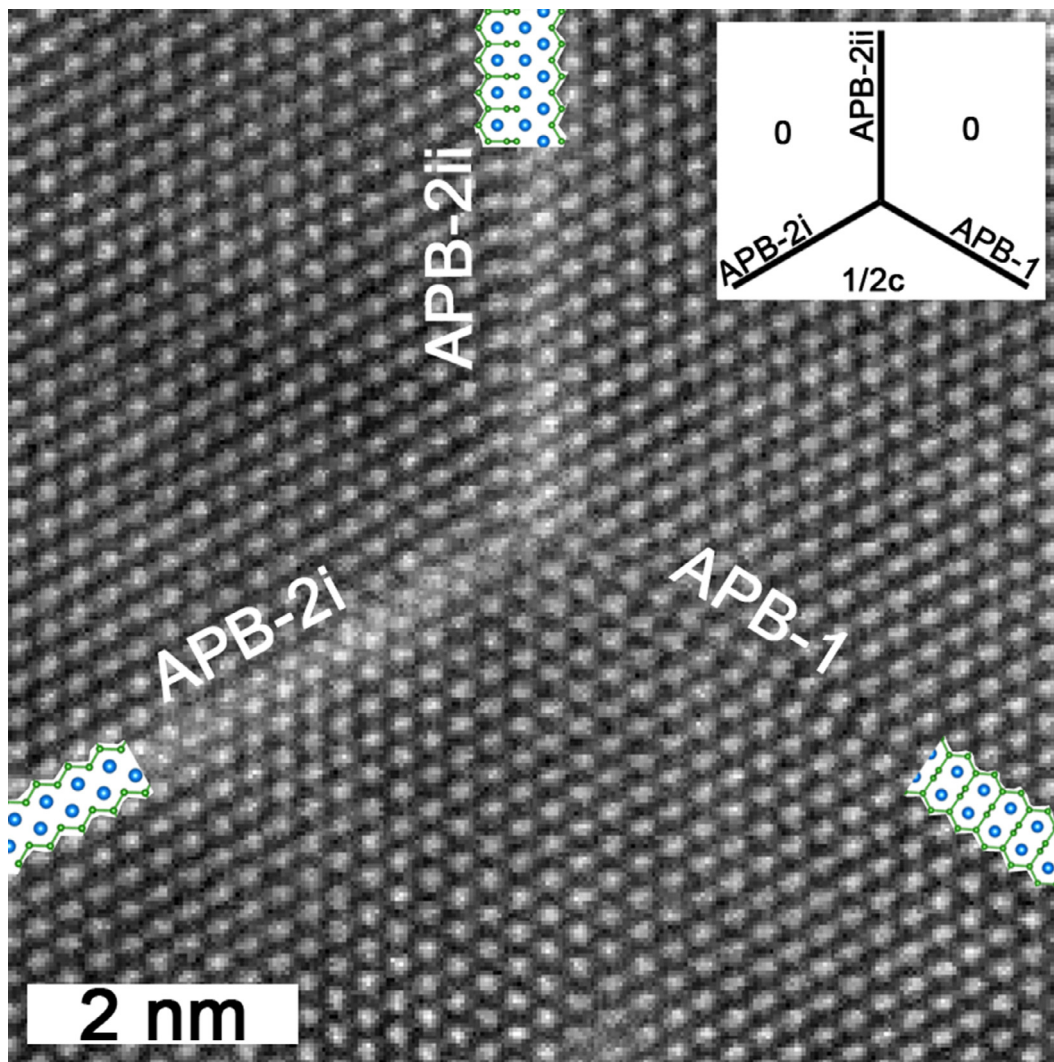
Fig. 6. The coexistence and accommodation of APB-1, APB-2i, and APB-2ii defects in the $CrB_{1.9}$ film. Inset shows the lattice shift along c-axis.
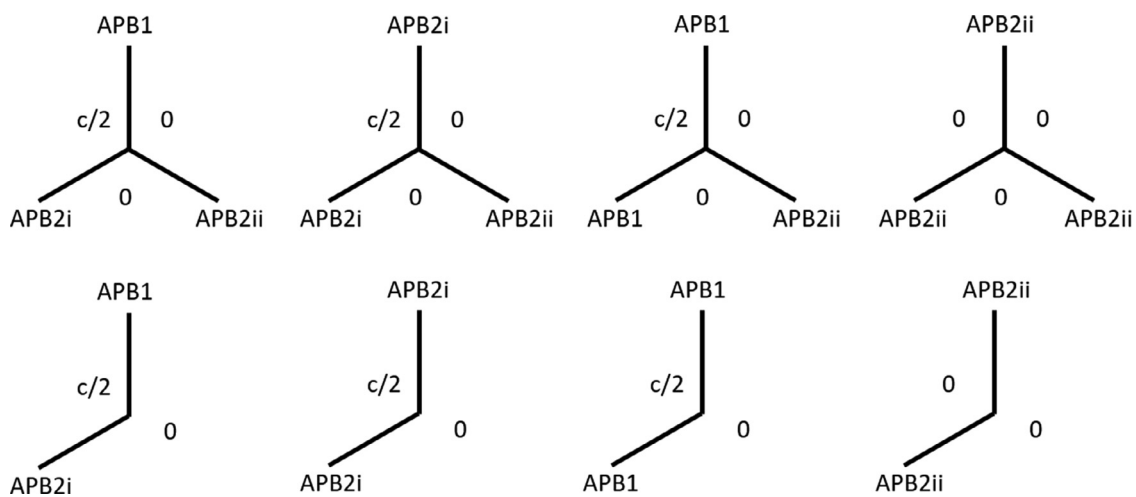

Fig. 7. Schematic illustration of possible 3- and 2-way APB interconnection configurations depicted with 120º angles.

tions. This was confirmed by observing the coexistence of various APB defect interconnection configurations in TMB_2 thin films.

Declaration of Competing Interest

None.

Supplementary materials

Supplementary material associated with this article can be found, in the online version, at doi:10.1016/j.mtla.2022.101478.

References

[1] R.G. Munro, Material properties of titanium diboride, J. Res. Natl. Inst. Stand. 105 (2000) 709–720.

[2] Y. Mu, K. Chen, W.J. Meng, F. Mei, Low temperature deposited titanium boride thin films and their application to surface engineering of microscale mold inserts, Microsyst. Technol. 18 (2012) 667–677.

[3] R.A. Andrievski, Nanostructured titanium, zirconium and hafnium diborides: the synthesis, properties, size effects and stability, Russ. Chem. Rev. 84 (2015) 540–545.

[4] M. Magnuson, L. Hultman, H. Högberg, Review of transition-metal diboride thin films, Vacuum 196 (2021) 110567.

[5] P.H. Mayrhofer, C. Mitterer, J.G. Wen, J.E. Greene, I. Petrov, Self-organized nanocolumnar structure in superhard TiB_2 thin films, Appl. Phys. Lett. 86 (2005) Article 131909.

[6] A. Mockuté, J. Palisaitis, B. Alling, P. Berastegui, E. Broitman, L.-Å. Näslund, N. Nedfors, J. Lu, J. Jensen, L. Hultman, J. Patscheider, U. Jansson, P.O.Å. Persson, J. Rosen, Age hardening in $(Ti_{1−x}Al_x)B_{2+\Delta}$ thin films, Scr. Mater. 127 (2017) 122–126.

[7] A. Mockuté, J. Palisaitis, N. Nedfors, P. Berastegui, E. Broitman, B. Alling, L.-Å. Näslund, L. Hultman, J. Patscheider, U. Jansson, P.O.Å. Persson, J. Rosen, Synthesis and characterization of $(Ti_{1−x}Al_x)B_{2+\Delta}$ thin films from combinatorial magnetron sputtering, Thin Solid Films 669 (2019) 181–187.

[8] C. Mitterer, Borides in thin film technology, J. Solid State Chem. 133 (1997) 279–291 J. Solid State Chem., 133 (1997), pp. 279-291.

[9] M.A. Nicolet, Diffusion barriers in thin films, Thin Solid Films 52 (1978) 415–443.

[10] M. Audronis, A. Leyland, A. Matthews, J.G. Wen, I. Petrov, Characterization studies of pulse magnetron sputtered hardceramic titanium diboride coatings alloyed with silicon, Acta Mater. 56 (16) (2008) 4172–4182.

[11] H. Euchner, P.H. Mayrhofer, H. Riedl, F.F. Klimashin, A. Limbeck, P. Polcik, S. Kolozsvari, Solid solution hardening of vacancy stabilized $Ti_xW_{1−x}B_2$, Acta Mater. 101 (2015) 55–61.

[12] V. Moraes, L. Zauner, T. Wojcik, M. Arndt, P. Polcik, H. Riedl, P.H. Mayrhofer, Thermally stable superhard diborides: an ab initio guided case study for V-W-diboride thin films, Acta Mater. 186 (2020) 487–493.

[13] C.G. Windsor, J.M. Marshall, J.G. Morgan, J. Fair, G.D.W. Smith, A. Rajczyk-Wryk, J.M. Tarragó, Design of cemented tungsten carbide and boride-containing shields for a fusion power plant, Nucl. Fus. 58 (7) (2018) 076014–076026.

[14] N.P. Bansal, Handbook of Ceramic Composites, Springer, Boston, MA, 2005.

[15] V. Moraes, C. Fuger, V. Paneta, D. Primetzhofer, P. Polcik, H. Bolvardi, M. Arndt, H. Riedl, P.H. Mayrhofer, Substoichiometry and tantalum dependent thermal stability of α-structured W-Ta-B thin films, Scr. Mater. 155 (2018) 5–10.

[16] N. Kalfagiannis, G. Volonakis, L. Tsetseris, S. Logothetidis, Excess of boron in TiB_2 superhard thin films: a combined experimental and ab initio study, J. Phys. D Appl. Phys. 44 (2011) Article 385402.

[17] R. Wiedemann, H. Oettel, M. Jerenz, Structure of deposited and annealed TiB_2 layers, Surf. Coat. Technol. 97 (1997) 313–321.

[18] C. López-Cartes, D. Martínez-Martínez, J.C. Sánchez-López, A. Fernández, A. García-Luis, M. Brizuela, J.I. Oñate, Characterization of nanostructured Ti–B–(N) coatings produced by direct current magnetron sputtering, Thin Solid Films 515 (2007) 3590–3596.

[19] J. Thörnberg, J. Palisaitis, N. Hellgren, F.F. Klimashin, N. Ghafoor, I. Zhirkov, C. Azina, J.-L. Battaglia, A. Kusiak, M.A. Sortica, J.E. Greene, L. Hultman, I. Petrov, P.O.Å. Persson, J. Rosen, Microstructure and materials properties of understoichiometric TiB_x thin films grown by HiPIMS, Surf. Coat. Technol. 404 (2020) Article 126537.

[20] M.M. Dorri, J. Thörnberg, N. Hellgren, J. Palisaitis, A. Petruhins, F. F.Klimashin, L. Hultman, I. Petrov, P.O.Å. Persson, J. Rosen, Synthesis and characterization of CrB_2 thin films grown by DC magnetron sputtering, Scr. Mater. 200 (2021) Article 113915.

[21] J. Thörnberg, B. Bakhit, J. Palisaitis, N. Hellgren, L. Hultman, G. Greczynski, P.O.Å. Persson, I. Petrov, J. Rosena, Improved oxidation properties from a reduced B content in sputter-deposited TiB_x thin films, Surf. Coat. Technol. 420 (2021) Article 127353.

[22] B. Bakhit, I. Petrov, J.E. Greene, L. Hultman, J. Rosén, G. Greczynski, Controlling the B/Ti ratio of TiB_x thin films grown by high-power impulse magnetron sputtering, J. Vac. Sci. Technol. A 36 (3) (2018) Article 030604.

[23] N. Hellgren, J. Thörnberg, I. Zhirkov, M.A. Sortica, I. Petrov, J. Greene, L. Hultman, J. Rosen, High-power impulse magnetron sputter deposition of TiB_x thin films: effects of pressure and growth temperature, Vacuum 169 (2019) Article 108884.

[24] N. Hellgren, A. Sredenschek, A. Petruins, J. Palisaitis, F.F. Klimashin, M.A. Sortica, L. Hultman, P.O.Å. Persson, J. Rosen, Synthesis and characterization of TiB_x (1.2≤ x≤ 2.8) thin films grown by DC magnetron co-sputtering from TiB_2 and Ti targets, Surf. Coat. Technol. 433 (2022) Article 128110.

[25] P. Malinovskis, J. Palisaitis, P.O.Å. Persson, E. Lewin, U. Jansson, Synthesis and characterization of $MoB_{2−x}$ thin films grown by nonreactive DC magnetron sputtering, J. Vac. Sci. Technol. A 34 (3) (2016) Article 031511.

[26] C. Fuger, R. Hahn, L. Zauner, T. Wojcik, M. Weiss, A. Limbeck, O. Hunold, P. Polcik, H. Ried, Anisotropic super-hardness of hexagonal $WB_{2±z}$ thin films, Mater. Res. Lett. 10 (2) (2022) 70–77.

[27] P.H. Mayrhofer, C. Mitterer, L. Hultman, H. Clemens, Microstructural design of hard coatings, Prog. Mater. Sci. 51 (2006) 1032–1114.

[28] P. Panjan, A. Drnovšek, P. Gselman, M. Cekada, M. Panjan, Review of growth defects in thin films prepared by PVD techniques, Coatings 10 (5) (2020) 447.

[29] B. Bakhit, J. Palisaitis, Z. Wu, M.A. Sortica, D. Primetzhofer, P.O.Å. Persson, J. Rosen, L. Hultman, I. Petrov, J.E. Greene, G. Greczynski, Age hardening in superhard ZrB_2-rich $Zr_{1−x}Ta_xB_y$ thin films, Scr. Mater. 191 (2021) 120–125.

[30] N. Nedfors, A. Mockute, J. Palisaitis, L.-Å.N P.O.Å.Persson, J. Rosen, Influence of pulse frequency and bias on microstructure and mechanical properties of TiB_2 coatings deposited by high power impulse magnetron sputtering, Surf. Coat. Technol. 304 (2016) 203–210.

[31] J. Palisaitis, M. Dahlqvist, A. J.Hall, J. Thörnberg, I. Persson, N. Nedfors, L. Hultman, J.E. Greene, I. Petrov, J. Rosen, P.O.Å. Perssona, Where is the unpaired transition metal in substoichiometric diboride line compounds? Acta Mater. 204 (2021) Article 116510.

[32] B. Paul, N.L. Okamoto, M. Kusakari, Z. Chen, K. Kishida, H. Inui, S. Otani, Plastic deformation of single crystals of CrB_2, TiB_2 and ZrB_2 with the hexagonal AlB_2 structure, Acta Mater. 211 (2021) Article 116857.

[33] V. Moraes, H. Riedl, C. Fuger, P. Polcik, H. Bolvardi, D. Holec, P.H. Mayrhofer, Ab initio inspired design of ternary boride thin films, Sci. Rep. 8 (2018) 9288.

[34] M. Dahlqvist, U. Jansson, J. Rosen, Influence of boron vacancies on phase stability, bonding and structure of MB_2 (M = Ti, Zr, Hf, V, Nb, Ta, Cr, Mo, W) with AlB_2 type structure, J. Phys. Condens. Matter 27 (2015) 435702.

[35] N. Nedfors, M. S, J. Palisaitis, P.O.Å. Persson, H. Lind, S. Kolozsvari, J.M. Schneider, J. Rosen, Influence of the Al concentration in Ti-Al-B coatings on microstructure and mechanical properties using combinatorial sputtering from a segmented TiB_2/AlB_2 target, Surf. Coat. Technol. 364 (2019) 89–98.

[36] N. Nedfors, D. Primetzhofer, I. Zhirkov, J. Palisaitis, P.O.Å. Persson, J.E. Greene, I. Petrov, J. Rosen, The influence of pressure and magnetic field on the deposition of epitaxial TiB_x thin films from DC magnetron sputtering, Vacuum 177 (2020) Article 109355.

[37] B. Bakhit, J. Palisaitis, J. Thörnberg, J. Rosen, P.O.Å. Persson, L. Hultman, I. Petrov, J.E. Greene, G. Greczynski, Improving the high-temperature oxidation resistance of TiB_2 thin films by alloying with Al, Acta Mater. 196 (2020) 677–689.

[38] B. Bakhit, J. Palisaitis, P.O.Å. Persson, B. Alling, J. Rosen, L. Hultman, I. Petrov, J.E. Greene, G. Greczynski, Self-organized columnar $Zr_{0.7}Ta_{0.3}B_{1.5}$ core/shell-nanostructure thin films, Surf. Coat. Technol. 401 (2020) Article 126237.

[39] J. Palisaitis, Use of cleaved wedge geometry for plan-view transmission electron microscopy sample preparation, Microsc. Res. Tech. 84 (2021) 3182–3190.

[40] S.J. Pennycook, L.A. Boatner, Chemically sensitive structure-imaging with a scanning transmission electron microscope, Nature 336 (1988) 565–567.

[41] E. Okunishi, I. Ishikawa, H. Sawada, F. Hosokawa, M. Hori, Y. Kondo, Visualization of light elements at ultrahigh resolution by STEM annular bright field microscopy, Microsc. Microanal. 15 (2009) 164–165.

[42] P.E. Blöchl, Projector augmented-wave method, Phys. Rev. B 50 (1994) 17953–17979.

[43] G. Kresse, D. Joubert, From ultrasoft pseudopotentials to the projector augmented-wave method, Phys. Rev. B 59 (1999) 1758–1775.

[44] G. Kresse, J. Hafner, Ab initio molecular dynamics for liquid metals, Phys. Rev. B 47 (1993) 558–561.

[45] G. Kresse, J. Furthmüller, Efficiency of ab-initio total energy calculations for metals and semiconductors using a plane-wave basis set, Comput. Mater. Sci. 6 (1996) 15–50.

[46] G. Kresse, J. Furthmüller, Efficient iterative schemes for ab initio total-energy calculations using a plane-wave basis set, Phys. Rev. B 54 (1996) 11169–11186.

[47] J.P. Perdew, K. Burke, M. Ernzerhof, Generalized gradient approximation made simple, Phys. Rev. Lett. 77 (1996) 3865–3868.

[48] H.J. Monkhorst, J.D. Pack, Special points for Brillouin-zone integrations, Phys. Rev. B 13 (1976) 5188–5192.

[49] M. Dahlqvist, B. Alling, I.A. Abrikosov, J. Rosén, Phase stability of Ti_2AlC upon oxygen incorporation: a first-principles investigation, Phys. Rev. B 81 (2010) Article 024111.

[50] M. Dahlqvist, B. Alling, J. Rosén, Stability trends of MAX phases from first principles, Phys. Rev. B 81 (2010) Article 220102.

[51] M.A. Zurbuchen, W. Tian, X.Q. Pan, D. Fong, S.K. Streiffer, M.E. Hawley, J. Lettieri, Y. Jia, G. Asayama, S.J. Fulk, D.J. Comstock, S. Knapp, A.H. Carim, D.G. Schlom, Morphology, structure, and nucleation of out-of-phase boundaries (OPBs) in epitaxial films of layered oxides, J. Mater. Res. 22 (2007) 1439–1471.

[52] O. Rubel, S.D. Baranovskii, Formation energies of antiphase boundaries in GaAs and GaP: an ab initio study, Int. J. Mol. Sci. 10 (2009) 5104–5114.

[53] A.C. Lin, M.M. Fejer, J.S. Harris, Antiphase domain annihilation during growth of GaP on Si by molecular beam epitaxy, J. Cryst. Growth 363 (2013) 258–263.

[54] Z. Wang, H. Guo, S. Shao, M. Saghayezhian, J. Li, R. Fittipaldi, A. Vecchione, P. Siwakoti, Y. Zhu, J. Zhang, E.W. Plummer, Designing antiphase boundaries by atomic control of heterointerfaces, Proc. Natl. Acad. Sci. 115 (38) (2018) 9485–9490.

[55] M. Haruta, H. Kurata, H. Komatsu, S.I Y.Shimakawa, Effects of electron channeling in HAADF-STEM intensity in La_2CuSnO_6, Ultramicroscopy 109 (2009) 361–367.

[56] R.G. Barnes, R.B. Creel, Chromium-like antiferromagnetic behavior of CrB_2, Phys. Lett. A 29 (1969) 203–204.